



## **Absolute stability mechanism of a swept cylinder laminar boundary layer with imposed spanwise periodic conditions**

E. Piot and G. Casalis

Citation: [Physics of Fluids](#) **21**, 064103 (2009); doi: 10.1063/1.3147933

View online: <http://dx.doi.org/10.1063/1.3147933>

View Table of Contents: <http://scitation.aip.org/content/aip/journal/pof2/21/6?ver=pdfcov>

Published by the [AIP Publishing](#)

---

### **Articles you may be interested in**

[Novel features of a fully developed mixing-layer between co-flowing laminar and turbulent Couette flows](#)

Phys. Fluids **26**, 031703 (2014); 10.1063/1.4868645

[Open-loop control of noise amplification in a separated boundary layer flow](#)

Phys. Fluids **25**, 124106 (2013); 10.1063/1.4846916

[On the relationship between the wall-shear-stress and transient-growth disturbances in a laminar boundary layer](#)

Phys. Fluids **22**, 054103 (2010); 10.1063/1.3415220

[Measurements in laminar regions of shock/shock and shock/boundary layer interaction over cylindrical leading edges, cone/cone and hollow cylinder flare configurations for DSMC/Navier-Stokes code validation](#)

AIP Conf. Proc. **585**, 699 (2001); 10.1063/1.1407628

[Linear and nonlinear development of localized disturbances in zero and adverse pressure gradient boundary-layers](#)

Phys. Fluids **10**, 1405 (1998); 10.1063/1.869665

---



## Launching in 2016!

The future of applied photonics research is here

**OPEN  
ACCESS**

**AIP** | APL  
Photonics

# Absolute stability mechanism of a swept cylinder laminar boundary layer with imposed spanwise periodic conditions

E. Piot<sup>a)</sup> and G. Casalis<sup>b)</sup>

ONERA DMAE, 2 av. Ed. Belin, BP 4025, 31 055 Toulouse Cedex, France

(Received 8 October 2008; accepted 2 May 2009; published online 9 June 2009)

The linear impulse response of a laminar three-dimensional boundary layer with imposed spanwise periodic conditions is theoretically analyzed. Because of the imposed spanwise periodicity, a unidirectional absolute instability is physically significant. The base flow is obtained through a direct numerical simulation of the flow along a swept cylinder, with periodic boundary conditions enforced at the spanwise boundaries. It is shown that this flow is absolutely stable. However, it exhibits crossflow modes of zero group velocity whose damping rate in time is quite slow. Moreover, these crossflow modes are spatially amplified. A direct numerical simulation of the same configuration but in the presence of surface roughness has enabled the observation of these traveling crossflow waves. The introduction of the roughness element in the computation creates initial transients that play the role of an impulselike forcing, which generates the traveling crossflow waves as predicted by the theoretical analysis. Depending on the roughness chordwise location, the frequency and damping rate in time of the crossflow waves change in agreement with the theoretical results. © 2009 American Institute of Physics. [DOI: 10.1063/1.3147933]

## I. INTRODUCTION

In a low-disturbance environment and on a smooth body, boundary layer transition to turbulence is generally due to the growth of instability waves within the laminar boundary layer. In the case of a swept boundary layer, these instability waves are the so-called crossflow waves, which develop in the negative pressure gradient region, close to the leading edge. The transition to turbulence can be decomposed into four steps. First, the crossflow waves are generated within the boundary layer through receptivity to various disturbances, such as free-stream turbulence or surface roughness. Next, the crossflow waves are linearly spatially amplified, until they reach a large enough amplitude to become subject to nonlinear evolution. This results in saturation of the primary waves and growth of harmonics. Finally, transition to turbulence is triggered by a powerful secondary instability of the saturated vortices. Comprehensive reviews for this transition scenario are given by Arnal<sup>1</sup> and Saric *et al.*,<sup>2,3</sup> among others. The three last stages of this transition are now quite well understood. Especially, calculations based on the nonlinear parabolized stability equations are successful in describing the crossflow wave growth, as demonstrated by Haynes and Reed<sup>4</sup> and direct numerical simulations (DNSs) are now able to capture the secondary instability mechanism, as described, for instance, by Bonfigli and Kloker.<sup>5</sup>

An alternative mechanism to saturation and secondary instability growth that could trigger the transition to turbulence is absolute instability. A flow is said to be absolutely unstable if initially localized disturbances spread upstream and downstream, thereby invading the entire physical domain of interest (see Ref. 6, for instance). For the rotating

disk problem, which has often been used as a model problem for swept wing flows, previous researchers have found that both a secondary instability (see Ref. 7) and an absolute instability (see Ref. 8) are possible. However, the rotating disk flow possesses an axial symmetry that is not present in swept wing boundary layers. Consequently, the criteria for the existence of absolute instability is more stringent in swept wing flows than in rotating disk flows: Lingwood<sup>9</sup> and Taylor and Peake<sup>10</sup> studied Falkner–Skan–Cooke and true swept wing boundary layers, and showed that these flows do not support an absolute instability, but do exhibit unidirectional absolute instability.

The present paper is focused on the first stage of the route to turbulence in a swept wing flow, i.e., the generation of the crossflow vortices. Over the past decades, many investigations have been carried out on this subject, mainly based on experiments or on theoretical approaches. Four main experimental programs have been performed, by Saric *et al.* on a swept wing (see Ref. 11), Kachanov *et al.* on a swept flat plate (see Ref. 12), Bippes *et al.* on various models with flat, concave and convex surfaces (see Ref. 13) and Takagi *et al.* on a swept cylinder (see Ref. 14). These experiments show that, even if unsteady crossflow waves can be observed, stationary crossflow waves dominate the transition process in low-disturbance environments, such as flight conditions. Moreover, it is shown that the primary cause of stationary crossflow vortices is surface roughness. Such a property has been checked by theoretical studies of receptivity in three-dimensional boundary layers. Especially, Crouch<sup>15</sup> and Choudhari<sup>16</sup> independently worked out the technique of finite Reynolds number theory (FRNT), which is in the same framework of the classical asymptotic receptivity theory of Goldstein<sup>17</sup> or Kerschen.<sup>18</sup> However, FRNT is based on parallel linearized stability equations in the vicinity of surface

<sup>a)</sup>Electronic mail: estelle.piot@onera.fr.

<sup>b)</sup>Electronic mail: gregoire.casalis@onera.fr.

disturbance rather than on triple-deck equations. Therefore, FRNT allows prediction of receptivity solutions at moderate Reynolds number in the vicinity of the surface disturbance. Bertolotti<sup>19</sup> recently extended this theory to take into account the mean-flow nonparallelism, by using an equivalent forcing method based on Fourier transforms. All these approaches demonstrate that the amplitude of stationary crossflow modes generated by the scattering of the mean flow by surface roughness is much higher than that of traveling waves due to the interaction of free-stream acoustic waves with the roughness, which explains the experimental observations.

Consequently, a numerical simulation dedicated to the study of surface roughness receptivity in a swept boundary layer is expected to exhibit only stationary crossflow waves, as far as no free-stream turbulence is imposed. Very few papers exist on this subject, as far as the authors are aware. Collis and Lele<sup>20</sup> computed the linearized Navier–Stokes solution in the vicinity of a small surface roughness on a swept leading edge, and compared it to FRNT results. More recently Schrader *et al.*<sup>21,22</sup> performed a DNS of the Falkner–Scan–Cooke flow on a swept flat plate in the presence of a small surface roughness that is sinusoidal in the spanwise direction. They compared their results to that obtained by the Bertolotti’s method. In both papers, only stationary crossflow waves can be observed. In a previous work,<sup>23</sup> we performed a DNS of the flow around a spanwise periodic roughness array on a swept cylinder. Even if all the boundary conditions were steady, an unsteadiness was observed in the flow. The present paper is thus dedicated to new direct numerical simulations of this configuration, and aims at explaining what is this unsteadiness and where it comes from.

This paper is organized as follows. First of all, the geometrical configuration and the numerical procedure are described (Sec. II). Then, the unsteadiness is presented and its nature is investigated with the help of a linear stability analysis of the flow without roughness (Sec. III). Next, we address the origin of the unsteadiness, and propose a scenario for its generation (Sec. IV). Finally, the major findings and conclusions of this study are summarized (Sec. V).

## II. FORMULATION

This section describes the geometry and the numerical tools used to obtain a DNS of the flow. The section ends with an explanation of the numerical procedure.

### A. Problem description

The flow over a swept cylinder is considered. This cylinder, shown in Fig. 1, and the flow conditions are similar to those chosen by Poll:<sup>24</sup> the cylinder radius is (dimensional quantities are indicated by an asterisk)  $R_c^*=0.1$  m, the sweep angle is  $\varphi=60^\circ$  and the incoming flow velocity is  $Q_\infty^*=50$  m s<sup>-1</sup>. The cylinder is idealized as having infinite span. This design is suited to study crossflow instability in the presence of considerable surface curvature. Two coordinate systems are shown in Fig. 1. Velocity components in the global coordinates are denoted by  $u$  in the vertical ( $x$ ) direction,  $v$  in the horizontal ( $y$ ) direction, and  $w$  in the spanwise

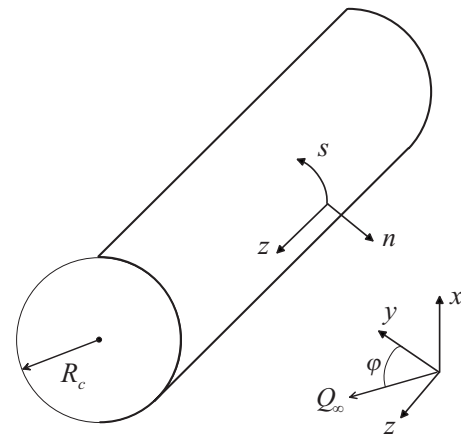


FIG. 1. Swept cylinder geometry.

( $z$ ) direction. The incoming velocity is given by  $[0, Q_\infty^* \cos(\varphi), Q_\infty^* \sin(\varphi)]$ . In the body-fixed coordinate system, the chordwise distance to the attachment line is denoted as  $s$ , the distance normal to the surface is  $n$ , and  $z$  is again the spanwise direction. Velocity components in the  $(s, n, z)$ -coordinate system are denoted by  $(v_s, v_n, w)$ . Infinite conditions are given by the static pressure  $P_\infty^*=101\,325$  Pa and the density  $\rho_\infty^*=1.18$  kg m<sup>-3</sup>. The free-stream incompressible flow over an infinite-span cylinder is given by an exact potential flow solution, which allows the computation of the expected laminar boundary layer with an in-house code. The boundary layer thickness along the attachment line, defined as the wall-normal distance for which both  $V_s^*$  and  $W^*$  reach 99.9% of their maximal value, is  $\delta_0^*=6.910 \cdot 10^{-4}$  m. In the following, the lengths in the wall-normal and spanwise directions are nondimensionalized by this reference length while the lengths in the chordwise direction are nondimensionalized by the cylinder radius  $R_c^*$  and expressed in degrees. The velocity components are nondimensionalized by the chordwise free-stream velocity  $U_\infty^*=Q_\infty^* \cos(\varphi)=25$  m s<sup>-1</sup>, and the pressure by  $\rho_\infty^* U_\infty^{*2}$ . The reference time scale is the free-stream convective scale  $R_c^*/U_\infty^*$ .

It must be pointed out that the considered boundary layer is unstable to crossflow instability since the flow is strongly accelerated with a rather large unit Reynolds number, but is stable to attachment line instability since the spanwise momentum-thickness Reynolds number is  $R_\theta=202$ , which is below the critical value of 230 given by the linear stability theory and observed in many experimental studies, as explained for instance by Arnal.<sup>1</sup>

The aim of the present paper is to study the stability properties of the boundary layer in the presence of a spanwise array of roughness elements. These ones have a parallelepipedic shape and are distributed along a line parallel to the attachment line. Two spatial configurations are studied: in case A, the chordwise center of the roughness array is located at  $s_R=7.6^\circ$ , while in case B it is located at  $s_R=13.8^\circ$ . The exact locations of the upstream and downstream wall of each roughness element ( $s_u$  and  $s_d$ , respectively) are given in Table I. The spanwise spacing between the roughness elements is  $\lambda_z=13$ . The choice of these specific values comes

TABLE I. Spatial characteristics of the roughness array in each studied configuration.  $s_u$ ,  $s_d$  and  $s_R$  denote the upstream, downstream and central chordwise locations of the roughness element.

	$s_u$	$s_d$	$s_R$	$\lambda_z$	$l_z/\lambda_z$	$h$	$Re_h$
Case A <sub>1</sub>						0.1	43.7
Case A <sub>2</sub>	7.3°	7.9°	7.6°	13	1/8	0.075	24.6
Case A <sub>3</sub>						0.05	11
Case B <sub>1</sub>					1/8	0.1	44.2
Case B <sub>2</sub>	13.5°	14.1°	13.8°	13	1/8	0.075	25.1
Case B <sub>3</sub>					3/8	0.1	44.2

from a previous study,<sup>23,25</sup> in which the roughness array had been designed to generate the stationary crossflow instabilities whose neutral stability line was the closest to the attachment line. [The neutral line for the steady  $\lambda_z=13$  crossflow wave is located at  $s=10.4^\circ$ , the neutral line for its first harmonic ( $\lambda_z/2$  spanwise wavelength) is located at  $s=14.3^\circ$ .] In the following, the roughness elements size will be varied, in both cases A and B. The corresponding height  $h$  and spanwise extent  $l_z$  are given in Table I, as well as the roughness Reynolds number  $Re_h$ , which is based on the roughness height and on the local velocity and kinematic viscosity at this height in the undisturbed boundary layer. It must be emphasized that the highest roughness elements are small enough not to trigger the transition to turbulence.

## B. Numerical methods

DNSs are performed to compute the flow around the cylinder, in both configurations: either the cylinder is smooth or there is a roughness array on its surface. The system of the compressible Navier–Stokes equations is solved numerically using the multipurpose in-house solver SABRINA.<sup>26</sup>

The Navier–Stokes equations are discretized using high-order numerical schemes and structured multiblock meshes. The spatial scheme is a classical fourth-order accurate centered explicit finite difference discretization, while a compact explicit third-order accurate Runge–Kutta algorithm is used for time advancement. Since such a centered scheme is not dissipative, it does not prevent the growth of spurious high-frequency numerical errors, and therefore requires a stabilization step. For that purpose, a tenth-order accurate symmetric linear filter is applied to the flow variables at each time step. The curvilinear extension strategy proposed by Visbal and Gaitonde<sup>27</sup> has been retained to handle complex geometries. The resulting scheme is quite classical in aeroacoustics, and has been extensively used for both aerodynamic and acoustic computations. Among other examples, this method has been used for direct numerical simulations of nonlinear global modes in hot jets, in Lesshafft *et al.*<sup>28</sup> The flow over the swept cylinder is modeled using an ideal gas where both the specific heat at constant pressure and the specific heat at constant volume are constant. The ratio of specific heat is 1.4, the Prandtl number is  $Pr^*=0.72$ . The dynamic viscosity is computed thanks to Sutherland’s law.

To simulate the effects of the periodic roughness array,

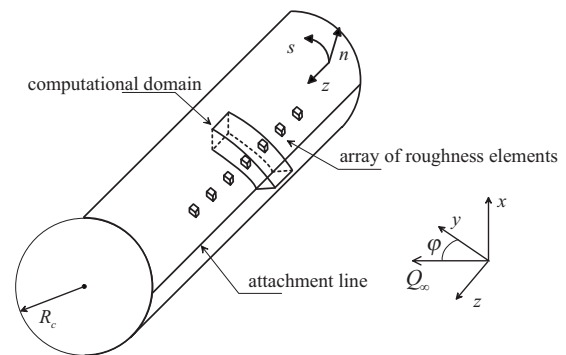


FIG. 2. Roughness array on the swept cylinder.

the computational domain contains a single roughness element centered at  $z=0$ , as shown in Fig. 2, and periodic boundary conditions are imposed in the spanwise direction at  $z=\pm\lambda_z/2$ . The same computational domain is used to compute the flow about the smooth cylinder.

Therefore, the three-dimensional curvilinear structured grid is made of eight subdomains, the eighth one representing the roughness element. In every case given in Table I, this subdomain is made of five points in the chordwise direction, seven points in the wall-normal direction; in cases A<sub>1</sub>, A<sub>2</sub>, A<sub>3</sub>, B<sub>1</sub>, and B<sub>2</sub>, nine points are used in the spanwise direction, while 27 points are used in case B<sub>3</sub>. Depending on whether the flow with or without roughness is computed, different conditions are enforced at the boundaries of this subdomain. In the case of the no-roughness computation, the subdomain No. 8 is connected to the other ones, and the flow is computed inside it. On the contrary, in the roughness case, adiabatic, no-slip conditions are enforced at the boundaries of this subdomain, and the flow is only computed on the seven other subdomains.

The computational domain is limited to the upper half of the flow field since the  $x=0$  plane is a plane of symmetry. An adiabatic, no-slip condition is imposed at the wall surface. Nonreflecting characteristic boundary conditions<sup>29</sup> are applied for the inflow boundary, which is located at  $n=20$ . The outflow condition is treated thanks to the use of a “sponge region” (progressive stretching of the computational grid in the chordwise direction) starting at  $s=23.7^\circ$ , which aims at damping the flow fluctuations. Finally, the whole mesh is made of about 3.5 millions points, with at least 61 points in the ( $n$ ) direction within the boundary layer at  $s=0^\circ$ . In previous studies,<sup>23,25</sup> the boundary layer computed around the smooth cylinder has been compared to the boundary layer predicted by a boundary layer code. It was shown that 61 points in the ( $n$ ) direction were enough to resolve correctly the boundary layer.

## C. Numerical procedure

To obtain the flow in the presence of the roughness array, a two-phases procedure is used, each phase being decomposed into an initialization step followed by the computation step:



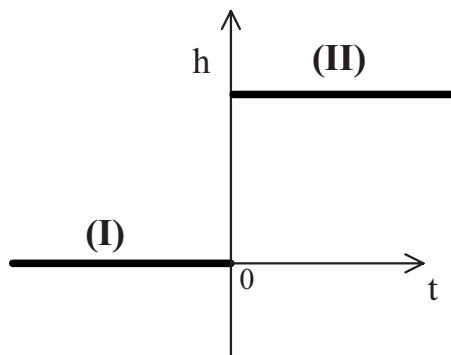


FIG. 3. Roughness height vs time. (I) corresponds to the no-roughness computation, (II) to the with-roughness computation.

- (I.1) The flow is initialized in the whole computational domain with the exact potential flow solution. This solution is valid for an incompressible flow, but for the considered incoming flow velocity of  $50 \text{ m s}^{-1}$ , the compressibility effects are weak and are not expected to influence significantly the properties of the studied flow.
- (I.2) Next, the Navier–Stokes equations are solved in the no-roughness configuration until a stationary solution is reached in the whole domain. This solution will be denoted as the base flow solution ( $V_s^{\text{cyl}}, V_n^{\text{cyl}}, W^{\text{cyl}}$ ) in the following sections. It depends only on the  $s$  and  $n$  locations.
- (II.1) In the second phase the roughness element is taken into account, i.e., no-slip conditions are imposed at the boundaries of the roughness subdomain. The previous base flow is used as an initial flow field. It must be noted that this initial flow field does not match the boundary conditions at the roughness wall.
- (II.2) The Navier–Stokes equations are solved in the with-roughness configuration. The obtained flow field is fully tridimensional.

The introduction of the roughness element in the computation can be summarized by the sketch in Fig. 3. The

computation without roughness [phase (I)] corresponds to  $t < 0$ , while the computation with roughness [phase (II)] corresponds to  $t > 0$ . The flow field at  $t=0^-$  is used to initialize the with-roughness computation.

Each  $q$  component of the flow (velocity, pressure, etc.) obtained in the with-roughness computation can be decomposed into a steady and an unsteady part:

$$q(s, n, z, t) = \langle q \rangle_0(s, n, z) + \tilde{q}(s, n, z, t), \quad (1)$$

where the steady part  $\langle q \rangle_0$  contains the base flow solution  $Q^{\text{cyl}}$ .

This paper focuses on the unsteady solution  $\tilde{q}$  only; Secs. III and IV will investigate the nature of this unsteadiness and its origin.

### III. NATURE OF THE UNSTEADINESS

#### A. Temporal and spatial structure

Figure 4 displays the time evolution of the  $v$  velocity component (each flow component has a similar time evolution) at various chordwise locations, from the starting ( $t=0$ ) of the with-roughness computation (see Fig. 3). Figure 4(a) corresponds to the case  $A_1$ , where the roughness element is centered at  $s=7.6^\circ$ , while Fig. 4(b) corresponds to the case  $B_1$ , where the roughness element is centered at  $s=13.8^\circ$ . The roughness size is the same in each case, as given in Table I.

In both cases, the flow is steady upstream of the roughness location [line  $s=0.1^\circ$  in Fig. 4(a) and lines  $s=0.1^\circ$  and  $s=10^\circ$  in Fig. 4(b)] and unsteady downstream of the roughness location [line  $s=10^\circ, 20^\circ$ , and  $23.5^\circ$  in Fig. 4(a) and lines  $s=15.6^\circ, 20^\circ$ , and  $23.5^\circ$  in Fig. 4(b)]. This unsteadiness propagates in the chordwise direction, and its amplitude increases with  $s$ . In case  $B_1$ , the unsteadiness is damped in time and at the end of the computation ( $t=2.4$ ), the flow is steady almost everywhere. On the contrary, in case  $A_1$  the damping rate is almost zero and the unsteadiness oscillation looks self-sustained.

Consequently, we focus on case  $A_1$  to investigate the spatial structure of the unsteadiness. The steady flow field  $\langle q \rangle_0$  [see Eq. (1)] is defined as the mean value in time of the

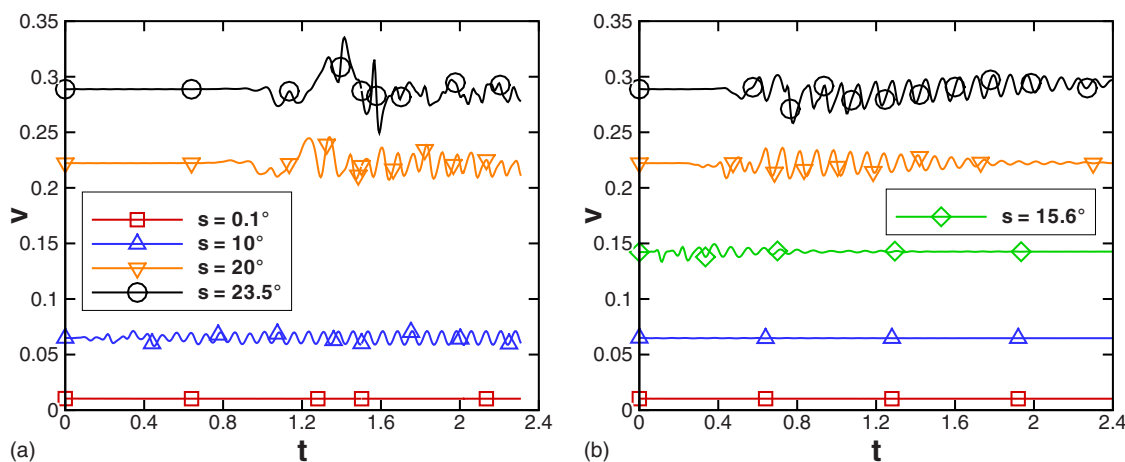


FIG. 4. (Color online)  $v$  velocity vs time, evaluated at  $n=1$ ,  $z=0$ , and at various chordwise locations. The symbols correspond to the same  $s$  values in (a) and (b), except that an additional chordwise location is plotted in (b). (a) Case  $A_1$ ;  $s_R=7.6^\circ$ . (b) Case  $B_1$ ;  $s_R=13.8^\circ$ .

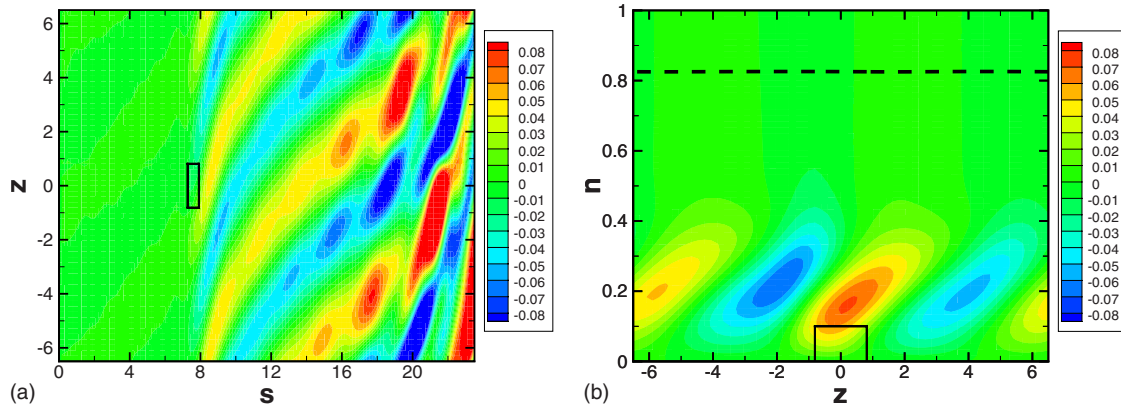


FIG. 5. (Color online) Fluctuating chordwise velocity  $\tilde{v}_s$  in the case  $A_1$ . The roughness top is at  $n=0.1$ . The location of the roughness element is represented by the black rectangle. The dashed line displays the local boundary layer thickness. (a)  $n=0.25$ . (b)  $s=15.6^\circ$ .

instantaneous flow field  $q$ . The computation is carried out until this steady flow field is spatially converged in the whole domain. A discrete Fourier transform of the fluctuating flow field  $\tilde{q} = q - \langle q \rangle_0$  shows that it is harmonic in time with a frequency  $f_{A_1} = 13.6 \pm 0.2$  (a more accurate value is unreachable with this method because of the Fourier resolution limit associated to such a short signal length):

$$\tilde{q}(s, n, z, t) = g(s, n, z) \cos[2\pi f_{A_1} t + \phi(s, n, z)].$$

Figure 5 displays the fluctuating chordwise velocity component in a plane  $(s, z)$  above the roughness top and in a plane  $(z, n)$  downstream of the roughness element. (The local boundary layer thickness is defined as the wall-normal distance for which both  $V_s^{\text{cyl}}$  and  $W^{\text{cyl}}$  reach 99% of their maximal value. This definition differs from that chosen to evaluate the reference length  $\delta_0^*$ .) Similar figures are obtained for the other velocity components. The fluctuating velocity can only be seen downstream of the roughness location. Moreover, the velocity oscillates in both  $s$  and  $z$  directions, and is amplified in the  $s$  direction. A spatial discrete Fourier transform has been performed in the  $z$  direction, which shows that, up to  $s=16.5^\circ$ , the fluctuating flow field is harmonic in  $z$  with a spanwise wavenumber equals to  $2\beta_z$ , where  $\beta_z$  stands for  $2\pi/\lambda_z$ . Further downstream, the spatial Fourier spectrum contains more wavenumbers, which is in agreement with the spatial evolution displayed in Fig. 5(a).

Finally, between  $s=s_R$  and  $s=16.5^\circ$  and after the transients, the fluctuating flow field evolves like a wave, and reads as

$$\tilde{q}(s, n, z, t) = \Re[\hat{q}(n) e^{i(k s + 2\beta_z z - \omega t)}], \quad (2)$$

where  $\Re$  stands for the real part,  $k$  is a complex chordwise wavenumber, which depends on  $s$ , and  $\omega = \omega_{A_1} = 2\pi f_{A_1}$ . A similar wavelike evolution is found in cases  $A_2$  and  $A_3$ : there is a change in the amplitude of the fluctuation (the smaller the roughness height, the smaller the amplitude), but the spanwise wavenumber is the same and there is almost no change in the frequency, as displayed in Table II. In cases  $B_1$ ,  $B_2$ , and  $B_3$ , the fluctuating flow field can be modeled in the same way, except that the circular frequency  $\omega$  has to be a complex number to take into account the damping in time.

The corresponding frequencies are given in Table II. Figure 6 displays the flow field obtained after the unsteadiness has been damped. It is shown in Ref. 25 that it corresponds to the steady crossflow wave with spanwise wavenumber  $\beta_z$ .

## B. Comparison to the linear stability theory

In order to find out the exact nature of the fluctuating flow field, a spatial linear stability analysis is performed on the base flow. The classical linear stability theory of parallel flows is used [the nonparallel effects do not influence significantly the comparison between the DNS results and the results of the linear stability analysis (see Ref. 25)]; this means that the base flow  $(V_s^{\text{cyl}}, W^{\text{cyl}})$  is assumed to be independent of  $s$  and that the wall-normal velocity  $V_n^{\text{cyl}}$  is neglected. At each chordwise location small fluctuations are decomposed into elementary instability waves

$$q^{iw}(s, n, z, t) = \check{q}(n) e^{i(\alpha s + \beta_z z - \omega t)} \quad (3)$$

of complex chordwise wavenumber  $\alpha$ , real spanwise wavenumber  $\beta$ , and real circular frequency  $\omega$ . The perturbation  $\check{q}$  satisfies the Orr–Sommerfeld equation for three-dimensional flows, which is solved after enforcement of appropriate boundary conditions at  $n=0$  and  $n=n_{\text{max}}$ .

The traveling crossflow waves  $q^{iw}$  associated with the spanwise wavenumber  $\beta=2\beta_z$  are computed for three frequencies in the range of the DNS frequency  $f_{A_1}$ . The chordwise evolution of the obtained chordwise wavenumber  $\alpha$  is plotted in Fig. 7. Both their real and imaginary parts are quite sensitive to the frequency. However, whatever the chosen frequency, the traveling crossflow wave is spatially amplified (i.e.,  $\alpha_i < 0$ ) for almost every chordwise location downstream of the roughness location in case  $A_1$  ( $s_R \approx 8^\circ$ ).

TABLE II. Frequency of the fluctuating flow field in each studied configuration. In the  $B$  cases the frequency has an imaginary part.

	Case $A_1$	Case $A_2$	Case $A_3$	Case $B_1$	Case $B_2$	Case $B_3$
$f$	13.6	13.7	13.9	$12-0.48i$	$12-0.55i$	$12-0.40i$

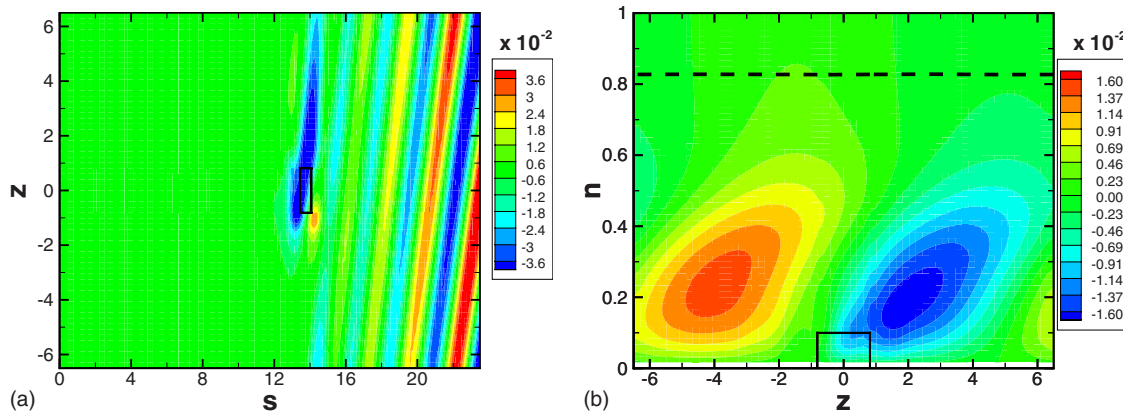


FIG. 6. (Color online) Steady chordwise velocity  $\langle v_s \rangle_0 - V_s^{cy1}$  in the case  $B_1$ . The roughness top is at  $n=0.1$ . The location of the roughness element is represented by the black rectangle. The dashed line displays the local boundary layer thickness. (a)  $n=0.25$ . (b)  $s=15.6^\circ$ .

As shown in Sec. III A, the DNS fluctuating flow field in case  $A_1$  behaves like a wave. Therefore, its spatial evolution is compared to that which is obtained by the Orr–Sommerfeld analysis. Figure 8 displays the amplitude and real part of the DNS chordwise velocity fluctuation, denoted as  $\hat{v}_s(n)\exp(iks)$  in Eq. (2). The results of the Orr–Sommerfeld analysis are also plotted; the  $s$ -dependency of the computed chordwise wavenumber  $\alpha$  is taken into account by plotting  $|\hat{v}_s(n)|\exp[-\int_{s_0}^s \alpha_i(\xi)d\xi]$  in Fig. 8(a) and  $\Re(\hat{v}_s(n)\cos[\int_{s_0}^s \alpha_r(\xi)d\xi])$  in Fig. 8(b). The traveling crossflow wave which is in best agreement with the DNS fluctuation is the one of frequency  $f=13.8$  concerning the chordwise amplification and the one of frequency  $f=13.6$  concerning the chordwise oscillation [that is why only this frequency is plotted in Fig. 8(b)]. Regardless of this slight uncertainty on the frequency, the comparison between the DNS and Orr–Sommerfeld results is very satisfactory. This means that the DNS fluctuation is a traveling crossflow wave, at least until  $s \approx 16.5^\circ$ . It is not true anymore downstream of this chordwise location, which agrees with the previous observation that then the DNS fluctuating flow field is not constituted by the  $2\beta_z$  spanwise harmonic only.

In order to confirm that the DNS fluctuation is indeed a traveling crossflow wave, the wall-normal evolution of  $\hat{q}$  is

compared in Fig. 9 to that of the eigenmode  $\hat{q}$  computed for  $f=13.8$ . The agreement is very good for each velocity component. The plots in Fig. 9 correspond to the chordwise location  $s=14^\circ$ , but a similar agreement is found at every chordwise location, up to  $s \approx 16.5^\circ$ .

Finally, all these results prove that the fluctuating flow field obtained in the case  $A_1$  of the DNS computations is a traveling crossflow wave of spanwise wavenumber  $2\beta_z$  and of frequency  $f \approx 13.8$ . It must also be noted that for cases  $A_2$  and  $A_3$ , the amplitude of the fluctuation differs from that obtained in case  $A_1$ , but not the wall-normal shape: it is always the same as the one of the crossflow eigenmode. In Sec. IV, we will investigate the origin of the unsteady wave obtained in the DNS.

#### IV. ORIGIN OF THE UNSTEADINESS

Two main hypotheses arise to explain the origin of the unsteadiness:

- (1) an instability of the recirculation zone around the roughness element and
- (2) an absolutelike instability mechanism of the base flow.

In this section each hypothesis is investigated.

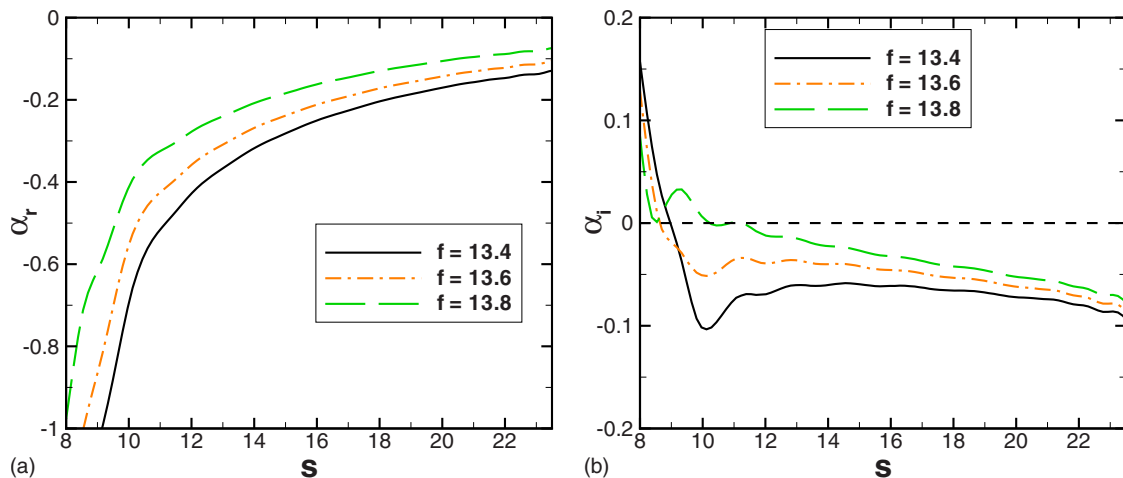


FIG. 7. (Color online) Real and imaginary parts of the chordwise wavenumber given by the Orr–Sommerfeld analysis, for three values of the frequency. The spanwise wavenumber is  $2\beta_z$ . (a) Real part of  $\alpha$ . (b) Imaginary part of  $\alpha$ .

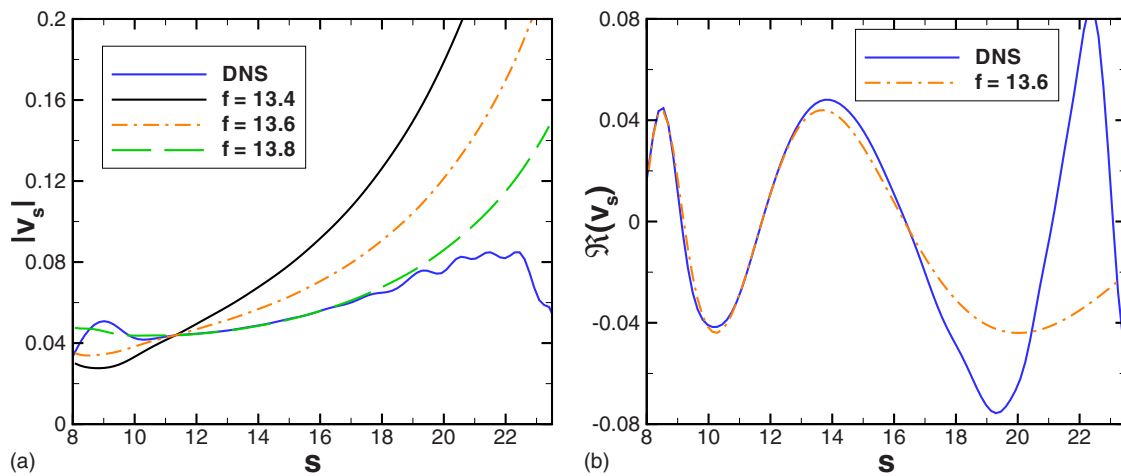


FIG. 8. (Color online) Comparison of the chordwise evolution between the  $A_1$ -DNS fluctuation and the traveling crossflow wave predicted by the Orr-Sommerfeld analysis. The wall-normal distance is  $n=0.25$ . (a) Chordwise amplification. (b) Chordwise oscillation.

### A. Instability of the recirculation zone?

Because of the grid topology, the roughness shape has a strong forward facing kink that can trap a recirculation zone under it. Many papers have studied the separation zones created by a two-dimensional (i.e., independent of  $z$ ) forward or backward facing step in a channel, but the studies in boundary layers are much more scarce, especially for three-dimensional roughness elements. To the authors' knowledge, only Smith and Walton<sup>30</sup> gave detailed information on the flow past a three-dimensional steep-edged roughness. Their study is based on the triple-deck formulation. They show that the length of the upstream separation region is about  $\text{Re}_h^{1/4}$ , but they do not give such a precise criterion for the downstream separation zone. They show moreover that the three-dimensional effects are only significant at the spanwise tips of the roughness element. The size of the separation regions can therefore be roughly estimated by the results on two-dimensional roughness elements. Such an experiment has been performed by Saric, Krutckoff, and Radezsky at the Arizona State University (private communication with Dr. Saric). They obtained a length of the downstream separation region that was about one to four times the roughness height

for roughness elements whose  $\text{Re}_h$  value was between 1 and 40. The length of the upstream separation region was about ten times smaller.

All these results show that in the present configuration, the length of the downstream separation region would be about a few  $h$ . However, the size of the computational cells around the roughness element is about  $16h$  in both  $s$  and  $z$  directions. The present mesh is therefore too coarse to capture the separated zone around the roughness element and any associated Kelvin-Helmholtz instability mechanism.

### B. Absolutelike instability of the base flow

As explained in Sec. III A, the spatiotemporal characteristics of the DNS unsteadiness do not depend on the roughness height, and the time evolution of the DNS fluctuation in case A looks like self-sustained oscillations, while in case B there is an exponential damping in time. These results make us study the linear response of the base flow to an initial forcing, which is at the source of the concept of absolute and convective instability.<sup>31</sup> For absolutely unstable flows the behavior of the response induced by an impulse forcing at a

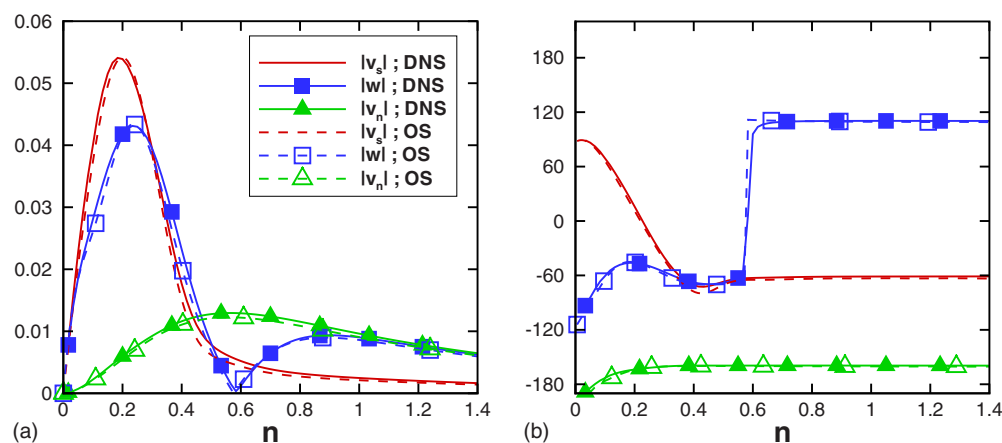


FIG. 9. (Color online) Comparison between the  $A_1$ -DNS fluctuating flow (solid lines) and the eigenfunction predicted by the linear stability theory (dashed lines) for a spanwise wavenumber of  $2\beta_z$  and a frequency of 13.8. The chordwise location is  $s=14^\circ$ . (a) Amplitudes, dimensionless. (b) Phases, in degrees.



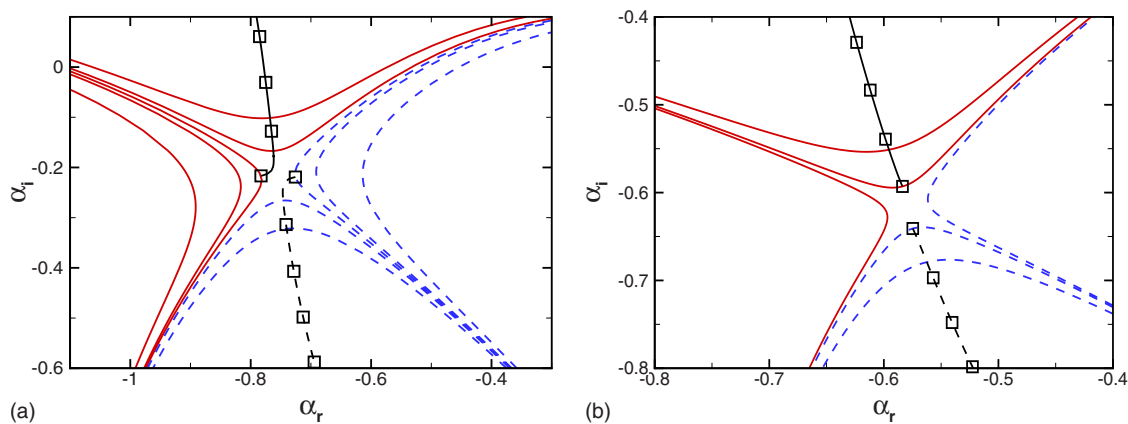


FIG. 10. (Color online) Mapping of the complex  $\omega$ -plane into the complex  $\alpha$ -plane. Results from the dispersion relation of the Orr–Sommerfeld equation, applied to the DNS-computed base flow. The spanwise wavenumber is  $\beta = 2\beta_z$ . (a)  $s = 7.6^\circ$ . (b)  $s = 13.8^\circ$ .

fixed spatial location is dominated by the absolute wavenumber corresponding to a zero group velocity. If the imaginary part of the associated *absolute frequency*  $\omega_0$  is negative, the flow is convectively unstable, while it is absolutely unstable if the imaginary part of  $\omega_0$  is positive. The absolute wavenumber and frequency correspond to a singularity of the dispersion relation that must fulfill a pinching requirement; such pinching points can be found by using the Briggs–Bers criterion.<sup>32,33</sup>

As mentioned in Sec. I, Lingwood<sup>9</sup> and Taylor and Peake<sup>10</sup> analyzed the linear impulse response of both Falkner–Skan–Cooke and true swept wing boundary layers. Because of the three-dimensional nature of the base flow, they searched for pinching points in both spanwise and chordwise wavenumber planes. Each wavenumber plane exhibits pinching points, but no simultaneous pinching was observed. That means that a true absolute instability does not exist for these boundary layers: the disturbance group velocity can go to zero in one direction but the disturbance will still convect in the other direction and therefore will leave the initial position free.

The absence of absolute instability in swept wing boundary layers was also experimentally investigated by White.<sup>34</sup> He considered a spanwise array of variable-amplitude leading-edge roughness and, during a single, continuous wind-tunnel run, increased the roughness amplitude from a flush configuration to an active roughness state and then came back to the initial inactive state where the roughness is flush with the wing surface. White checked that the flow was laminar in the initial inactive configuration, then became turbulent when the roughness were activated, and finally reverted to a laminar state when the roughness amplitude was decreased to the original inactive amplitude. The absence of a hysteresis effect proved that the flow was absolutely stable.

In White’s configuration the roughness is spanwise periodic, as in the present study, but the roughness elements have a finite spanwise extent. The forcing with the variable-amplitude roughness bears a resemblance with that obtained in the present DNS (see the sketch in Fig. 3), except that the step-function-type forcing is necessarily smoother in an experiment than in a numerical simulation. On the other hand,

White was looking for an absolute instability of a basic flow which had been nonlinearly modified by the roughness-induced stationary crossflow waves. Therefore, the spanwise spacing between the roughness elements was chosen in order to force the most amplified stationary mode, which is not the case in the present simulation: the obtained crossflow waves are only weakly amplified. Our DNS thus represents a subtly different situation than White’s experiments.

The present configuration is also different from that studied by Lingwood or Taylor and Peake: as periodicity is enforced in the spanwise direction, the spanwise wavenumber is fixed to a real multiple of  $\beta_z$  and an impulse response analysis in the spanwise wavenumber plane is meaningless. Indeed, our configuration behaves as if there was a spanwise-infinite system of excitation: any disturbance will build on itself along the span. Consequently, the studied configuration is much more like that of a rotating flow, for which only the chordwise wavenumber plane has to be studied because the axial symmetry forces  $\beta$  to be a real number (see Ref. 8).

The response of the DNS-computed base flow ( $V_s^{cyl}, 0, W_s^{cyl}$ ) to an initial forcing is thus studied by using the Briggs–Bers criterion in the complex chordwise wavenumber plane only, for the fixed spanwise wavenumber  $2\beta_z$ . The dispersion relation of the three-dimensional Orr–Sommerfeld equation is used. This analysis is performed at two chordwise locations:  $s = 7.6^\circ$  and  $s = 13.8^\circ$ . The map of the  $\omega$  plane into the  $\alpha$  plane under the dispersion relation is shown in Fig. 10, for both chordwise locations. The lines without symbols correspond to the spatial branches obtained by varying  $\omega$  along straight lines parallel to the real  $\omega$ -axis, while for the lines with symbols  $\omega_r$  is kept constant and  $\omega_i$  is increased. Solid lines correspond to the crossflow mode and dashed lines to another mode of the spectrum. Figure 10 shows that a saddle point forms in the complex  $\alpha$  plane. Moreover, its branches originate from distinct halves of the  $\alpha$  plane, as clearly shown by the lines with symbols. According to the Briggs–Bers method, this ensures that this pinch point  $\alpha_0$  is the absolute wavenumber associated to the long-time behavior of the impulse response. The corresponding branch point is  $\omega_0 = 88 - 0.56i$  ( $f_0 = 14 - 0.09i$ ) for  $s = 7.6^\circ$  and  $\omega_0 = 78.5 - 3.89i$  ( $f_0 = 12.5 - 0.62i$ ) for  $s = 13.8^\circ$ . As the imagi-

nary part of  $\omega_0$  is negative, the flow is convectively unstable at both chordwise locations. However, at  $s=7.6^\circ$  the imaginary part of the absolute frequency is very low, which means that the damping in time of the impulse response will be weak.

All these results match with the time characteristics of the DNS unsteadiness:  $s=7.6^\circ$  corresponds to the roughness location in case A, i.e., to the location where perturbations are introduced at the beginning of the with-roughness computation. Indeed, as explained in Sec. II C, the with-roughness computation is initialized with the no-roughness flow field, i.e.,  $(V_s^{\text{cyl}}, V_n^{\text{cyl}}, W^{\text{cyl}})$ , which is nonzero at the roughness wall. Consequently, strong initial transients arise because of the necessary development of the complex flow pattern that allows the flow to wrap around the roughness element. These transients play the role of a causal forcing, which is not strictly speaking impulsive since these transients do not disappear instantaneously, but is almost impulsive since the flow structure around the roughness element is fully established long before the end of the simulation. It has been shown that the absolute frequency predicted by the impulse response analysis is  $f_0=14-0.09i$ . This value differs from the  $f_{A_1}$ ,  $f_{A_2}$ , or  $f_{A_3}$  values (given in Table II) by less than 3%. On the other hand,  $s=13.8^\circ$  corresponds to the roughness location in case B. The absolute frequency predicted by the impulse response analysis is  $f_0=12.5-0.62i$ , which differs from the  $f_{B_1}$ ,  $f_{B_2}$ , or  $f_{B_3}$  values (see Table II) by less than 4%. These slight differences may be due to the nonparallel and surface curvature effects, which are taken into account in the DNS computations, but not in the linear impulse response analysis.

Moreover, it has been seen that the DNS unsteadiness is the same traveling crossflow wave in each case  $A_1$ ,  $A_2$ , and  $A_3$ , but with a different amplitude (this is also true for cases  $B_1$ ,  $B_2$ , and  $B_3$ ). This behavior is in agreement with a linear impulse response of various level, associated with the various strengths of the transients due to the initialization process: the smaller the roughness element, the weaker the adjustments needed to fulfill the no-slip boundary condition.

All these results let us think that the origin of the traveling crossflow wave observed in the DNS computations is a “quasi-absolute” instability mechanism of the no-roughness flow field: these instability waves are convectively unstable and absolutely stable, but with an imaginary part of the absolute frequency (i.e., their damping rate in time) which is small enough to make them visible in the DNS computations.

Finally, a discussion can be made on an eventual instability of the numerical computation. Buell and Huerre<sup>35</sup> showed that global self-sustained oscillations can be observed in numerical simulations of flows that are convectively unstable everywhere. This spurious global behavior is due to the outflow numerical boundary conditions that create destabilizing pressure feedback loops. Cossu and Loiseleux<sup>36</sup> studied the influence of finite difference numerical schemes on the capture of absolute or convective instabilities in open flows. They showed that sometimes the choice of the scheme can make a convective instability looks absolute, and vice versa. We do not think that such an issue is in stake in the

present computations, because of the very good agreement obtained between the observations in the DNS and the predictions of the linear impulse theory.

## V. CONCLUSIONS

The stability of the laminar boundary layer along a swept cylinder has been investigated both numerically and theoretically, in the situation where the boundary conditions impose a spanwise periodicity. The boundary layer flow has been computed through a DNS of the Navier–Stokes equations, which has been validated by comparing its result with that of a boundary layer code. A second computation has been performed to obtain the flow in the presence of a surface roughness element. Periodic boundary conditions are enforced at the spanwise boundaries of the computational domain to model a spanwise roughness array. The roughness element has a parallelepipedic shape and is small enough not to trigger the transition to turbulence. Downstream of the roughness element the flow exhibits unsteady waves, which are self-sustained or quickly damped in time depending on the roughness chordwise location. A spatial linear stability analysis of the boundary layer flow (i.e., the flow around the smooth cylinder) has proved that these unsteady waves are traveling crossflow waves with a spanwise wavelength half as large as the spanwise size of the computational domain.

The origin of these traveling crossflow waves has been investigated theoretically. The linear impulse response of the flow around the smooth cylinder has been analyzed, by taking into account the imposed spanwise periodicity. Therefore, the spanwise wavenumber must be an integer multiple of the wavenumber associated with the spanwise extent of the computational domain. A unidirectional absolute instability analysis is thus significant, since a forcing-induced disturbance that convects in the spanwise direction while growing in time at a fixed chordwise position, will build on itself when reaching one of the spanwise boundary of the computational domain. It has been showed that the flow around the smooth cylinder exhibits crossflow modes of zero group velocity, whose associated absolute frequency has a negative imaginary part; consequently, this flow is absolutely stable. However, there is a chordwise location where the imaginary part of the absolute frequency is very close to zero. This location is precisely the one where the presence of a roughness element generates self-sustained crossflow waves in the DNS computations. Moreover, the frequency of these traveling crossflow waves matches the real part of the absolute frequency obtained from the linear impulse response analysis of the flow around the smooth cylinder. A similar agreement is found between the frequency and damping rate in time of the crossflow waves generated by a roughness located more downstream, and the absolute frequency obtained at the corresponding chordwise location. Additional DNS computations have shown that a change in the roughness height or spanwise extent had an impact on the amplitude of the generated crossflow waves, but not on their spatiotemporal behavior. In fact, when the DNS computation is initialized with the smooth cylinder flow, strong initial transients arise

because of the necessary development of the complex flow pattern that allows the flow to wrap around the roughness element. These transients are causal (they appear at the beginning of the simulation with the roughness element), and are almost impulsive since they disappear as soon as the flow structure around the roughness surface is established. Our guess is that such transients play the role of an impulse forcing, which generates the traveling crossflow modes through the linear impulse response mechanism found out for the studied boundary layer flow.

Up until now, such an absolutelike instability mechanism has not been observed in experiments. However, it must be noted that the present configuration possesses distinctive features that are inherent to a numerical simulation and could hardly be obtained in experiments. First, the roughness elements appear instantaneously in the boundary layer, while in most experiments roughness elements are static. A near-impulsive forcing can be attempted in experiments by implementing variable-amplitude roughness, but such an introduction of the roughness element would never be as abrupt as in the simulation. Second, perfectly periodic spanwise boundary conditions are imposed in the numerical simulation, which is unachievable in practice. Moreover, such a condition implies that the forcing induced by the transients is exactly the same all along the infinite span. Finally, the physical conditions used in the present simulation (pressure gradient,  $N$  factor of the crossflow modes) do not correspond to the most amplified crossflow modes and are consequently less easily observable in experiments, and the absolute mode supported by the studied flow is not unstable but only marginally stable.

## ACKNOWLEDGMENTS

The assistance of Marc Terracol in the use of the DNS code is gratefully acknowledged.

<sup>1</sup>D. Arnal, "Boundary layer transition: Predictions based on linear theory," AGARD FDP/VKI Special Course on "Progress in Transition Modelling," AGARD Report No. R-793, VKI, Brussels, Belgium, 1993, pp. 2.1–2.63.

<sup>2</sup>W. S. Saric, H. L. Reed, and E. B. White, "Stability and transition of three-dimensional boundary layers," *Annu. Rev. Fluid Mech.* **35**, 413 (2003).

<sup>3</sup>W. S. Saric and H. L. Reed, "Crossflow instabilities-theory and technology," 41st Aerospace Sciences Meeting and Exhibit, Reno, NV, 2003, Paper No. AIAA-2003-771.

<sup>4</sup>T. S. Haynes and H. L. Reed, "Simulation of swept-wing vortices using nonlinear parabolized stability equations," *J. Fluid Mech.* **405**, 325 (2000).

<sup>5</sup>G. Bonfigli and M. Kloker, "Secondary instability of crossflow vortices: validation of the stability theory by direct numerical simulation," *J. Fluid Mech.* **583**, 229 (2007).

<sup>6</sup>P. Huerre and M. Rossi, *Hydrodynamics and Nonlinear Instabilities* (Cambridge University Press, Cambridge, England, 1998), Chap. 2.

<sup>7</sup>Y. Kohama, "Study on boundary layer transition of a rotating disk," *Acta Mech.* **50**, 193 (1984).

<sup>8</sup>R. J. Lingwood, "Absolute instability of the boundary layer on a rotating disk," *J. Fluid Mech.* **299**, 17 (1995).

<sup>9</sup>R. J. Lingwood, "On the impulse response for swept boundary-layer flows," *J. Fluid Mech.* **344**, 317 (1997).

<sup>10</sup>M. J. Taylor and N. Peake, "The long-time behaviour of incompressible

swept-wing boundary layers subject to impulsive forcing," *J. Fluid Mech.* **355**, 359 (1998).

<sup>11</sup>M. S. Reibert and W. S. Saric, "Review of swept-wing transition," 28th Fluid Dynamics Conference, Snowmass Village, CO, 1997, Paper No. AIAA-97-1816.

<sup>12</sup>Y. S. Kachanov, "Three-dimensional receptivity of boundary layers," *Eur. J. Mech. B/Fluids* **19**, 723 (2000).

<sup>13</sup>H. Bippes, "Basic experiments on transition in three-dimensional boundary layers dominated by crossflow instabilities," *Prog. Aerosp. Sci.* **35**, 363 (1999).

<sup>14</sup>S. Takagi and N. Itoh, "Observation of traveling waves in the three-dimensional boundary layer along a yawed cylinder," *Fluid Dyn. Res.* **14**, 167 (1994).

<sup>15</sup>J. D. Crouch, "Receptivity of three-dimensional boundary layers," 31st Aerospace Science Meeting and Exhibit, Reno, NV, 11–14 January 1993, Paper No. AIAA-93-0074.

<sup>16</sup>M. Choudhari, "Roughness-induced generation of crossflow vortices in three-dimensional boundary layers," *Theor. Comput. Fluid Dyn.* **6**, 1 (1994).

<sup>17</sup>M. E. Goldstein, "Scattering of acoustic waves into Tollmien-Schlichting waves by small streamwise variations in surface geometry," *J. Fluid Mech.* **154**, 509 (1985).

<sup>18</sup>E. Kerschen, "Boundary layer receptivity," AIAA 12th Aeroacoustics Conference, San Antonio, TX, 1989, Paper No. AIAA-89-1109.

<sup>19</sup>F. P. Bertolotti, "Receptivity of three-dimensional boundary-layers to localized wall roughness and suction," *Phys. Fluids* **12**, 1799 (2000).

<sup>20</sup>S. S. Collis and S. K. Lele, "Receptivity to surface roughness near a swept leading edge," *J. Fluid Mech.* **380**, 141 (1999).

<sup>21</sup>E. Piot and L. U. Schrader, "Receptivity of three-dimensional boundary layers to surface roughness," ERCOFTAC Bulletin No. 74, 2007.

<sup>22</sup>L. U. Schrader, L. Brandt, and D. S. Henningson, "Receptivity mechanisms in three-dimensional boundary-layer flows," *J. Fluid Mech.* **618**, 209 (2009).

<sup>23</sup>E. Piot, G. Casalis, and M. Terracol, "Direct numerical simulation of the crossflow instabilities induced by a periodic roughness array on a swept cylinder: Receptivity and stability investigations," 37th Fluid Dynamics Conference, Miami, FL, 2007, Paper No. AIAA-2007-3976.

<sup>24</sup>D. I. A. Poll, "Some observations of the transition process on the windward face of a long yawed cylinder," *J. Fluid Mech.* **150**, 329 (1985).

<sup>25</sup>E. Piot, "Simulation numérique directe et analyse de stabilité de couches limites laminaires en présence de micro-rugosités," Ph.D. thesis, Institut National Supérieur de l'Aéronautique et de l'Espace, 2008.

<sup>26</sup>M. Terracol, "Développement d'un solveur pour l'aéroacoustique numérique: sAbrinA," Rapport technique ONERA Technical Report No. RT 5/07383 DSNA, 2003.

<sup>27</sup>M. R. Visbal and D. V. Gaitonde, "On use of higher-order finite-difference schemes on curvilinear and deforming meshes," *J. Comput. Phys.* **181**, 155 (2002).

<sup>28</sup>L. Lesshafft, P. Huerre, P. Sagaut, and M. Terracol, "Nonlinear global modes in hot jets," *J. Fluid Mech.* **554**, 393 (2006).

<sup>29</sup>K. W. Thompson, "Time dependent boundary conditions for hyperbolic systems," *J. Comput. Phys.* **68**, 1 (1987).

<sup>30</sup>F. T. Smith and A. G. Walton, "Flow past a two- or three-dimensional steep-edged roughness," *Proc. R. Soc. London, Ser. A* **454**, 31 (1998).

<sup>31</sup>P. Huerre and P. A. Monkewitz, "Local and global instabilities in spatially developing flows," *Annu. Rev. Fluid Mech.* **22**, 473 (1990).

<sup>32</sup>R. J. Briggs, *Electron-Stream Interaction with Plasmas* (MIT Press, Cambridge, MA, 1964).

<sup>33</sup>A. Bers, *Handbook of Plasma Physics* (North-Holland, Amsterdam, 1983), Chap. 3.2, Vol. 1.

<sup>34</sup>E. B. White, "Breakdown of crossflow vortices," Ph.D. thesis, Arizona State University, 2000.

<sup>35</sup>J. C. Buell and P. Huerre, "Inflow/outflow boundary conditions and global dynamics of spatial mixing layers," Studying Turbulence Using Numerical Simulation Databases, 2. Proceedings of the 1988 Summer Program, pp. 19–27, Center for Turbulence Research Technical Report No. CTR-S88, 1988.

<sup>36</sup>C. Cossu and T. Loiseux, "On the convective and absolute nature of instabilities in finite difference numerical simulations of open flows," *J. Comput. Phys.* **144**, 98 (1998).